



This open access document is posted as a preprint in the Beilstein Archives at <https://doi.org/10.3762/bxiv.2021.5.v1> and is considered to be an early communication for feedback before peer review. Before citing this document, please check if a final, peer-reviewed version has been published.

This document is not formatted, has not undergone copyediting or typesetting, and may contain errors, unsubstantiated scientific claims or preliminary data.

**Preprint Title** A novel MoS<sub>2</sub>/ tourmaline /graphene ternary composite with enhanced visible-light photocatalytic property

**Authors** Mengjia Liu, Changqiang Yu, Xiaowen Liu, Peng Wang and Yingjie Chen

**Publication Date** 25 Jan. 2021

**Article Type** Full Research Paper

**Supporting Information File 1** Supporting Informatio1.docx; 493.1 KB

**ORCID® IDs** Xiaowen Liu - <https://orcid.org/0000-0001-7793-5048>

License and Terms: This document is copyright 2021 the Author(s); licensee Beilstein-Institut.

This is an open access work under the terms of the Creative Commons Attribution License (<https://creativecommons.org/licenses/by/4.0>). Please note that the reuse, redistribution and reproduction in particular requires that the author(s) and source are credited and that individual graphics may be subject to special legal provisions.

The license is subject to the Beilstein Archives terms and conditions: <https://www.beilstein-archives.org/xiv/terms>.

The definitive version of this work can be found at <https://doi.org/10.3762/bxiv.2021.5.v1>

# **A novel MoS<sub>2</sub>/ tourmaline /graphene ternary composite with enhanced visible-light photocatalytic property**

1<sup>st</sup> Mengjia Liu<sup>1,2</sup>, 2<sup>nd</sup> Changqiang Yu<sup>1,2</sup>, Xiaowen Liu<sup>\*1,2</sup>, Peng Wang<sup>1,2</sup>, Yingjie Chen<sup>1,2</sup>

Address: School of Minerals Processing and Bioengineering, Central South University, Changsha 410083, China.<sup>2</sup> Key Laboratory for Mineral Materials and Application of Hunan Province, Central South University, Changsha 410083, China

Email: Xiaowen Liu - lxwdr@csu.edu.cn

\* Corresponding author at School of Minerals Processing and Bioengineering, Central South University, Changsha 410083, China.

## **Abstract**

In this study, MoS<sub>2</sub>-graphene-tourmaline (MoS<sub>2</sub>-GR-T) composite photocatalyst was successfully synthesized via one-step hydrothermal method. Raman spectra revealed that graphene oxide was reduced to graphene. Scanning electron microscopy images showed that MoS<sub>2</sub> was dispersed well on graphene. Transmission electron microscope images showed that MoS<sub>2</sub> and tourmaline contacted well with graphene. Analysis of UV-visible diffuse reflectance spectra implied that the bandgap energies of MoS<sub>2</sub>, MoS<sub>2</sub>-T and MoS<sub>2</sub>-GR-T samples were 2.01 eV, 1.91 eV and 1.79 eV, respectively. The photocatalytic performances are evidenced under Xenon lamp irradiation utilizing

Rhodamine B dye as the model compound. Compared with MoS<sub>2</sub> and MoS<sub>2</sub>-GR, the MoS<sub>2</sub>-graphene-tourmaline (MoS<sub>2</sub>-GR-T) composites exhibited the excellent photocatalytic activity for the degradation about irradiating for 60 min were 93.9% under visible-light. The enhanced photocatalytic activity of MoS<sub>2</sub>-GR-T composite could be attributed to the exposed adsorption-photocatalytic active sites, the improved light adsorption ability and the promoted charge separation efficiency. The introduction of tourmaline reduced the band gap explored by analysis of UV-visible diffuse reflectance spectra. This work demonstrated that the charge efficiency of photocatalysts could be promoted by coupling both metal-free co-catalyst and polar mineral.

## Keywords

MoS<sub>2</sub>-GR-T composite; Hydrothermal method; Photocatalytic property; Rhodamine R; Visible light

## Introduction

Recently, photocatalytic degradation and complete mineralization of toxic organic compounds in water, soil, and air in the presence of semiconductor powders have gained increased attention [1-2]. Owing to their special properties, metal sulfides have been widely applied in the fields of solar cell [3-4], lithium-ion battery [5-8], sensor [9-10], photocatalytic hydrogen evolution [11-12], photocatalytic organics synthesis [13-14] and photocatalytic degradation [15-16]. Among of metal sulfides, MoS<sub>2</sub> are widely used in the process of organic dyes degradation because of the peculiar advantages about the hierarchical structure, narrow band gap energy ( $E_g=1.2$  eV-1.9 eV) [17-18], prominent

viability against photocorrosion [19-20], extraordinary electronic and optical properties [21-24].

However, fast recombination of the photo-generated  $e^-/h^+$  pairs restricted its photocatalytic property [25]. There has been significant progress in solving the aforementioned problems. Co-catalysts [15, 26-28] and supporting materials [20, 29-30] were regarded as effective strategies to improve the photocatalytic property of  $\text{MoS}_2$ . The co-catalysts were studied based on the heterojunction exist in the interface of catalysts, which could transfer photo-induced  $e^-/h^+$  pairs to promote the photocatalytic property [28, 31]. While, supporting materials were used to disperse catalysts to expose more active sites due to its large surface area [20, 29]. GR is a kind of two-dimensional carbon species and is available to use as supporting and electron-transfer materials in photocatalytic field because of its higher specific surface area and outstanding electronic properties [32-34].  $\text{MoS}_2$ -graphene composite was studied by many researchers and the composite showed enhanced photocatalytic property [35-38].

Tourmaline (T) is a kind of earth abundant boronsilicate mineral with rhombohedral or trigonal structure,  $R3m$  space group, generally written as  $\text{XY}_3\text{Z}_6(\text{T}_6\text{O}_{18})(\text{BO}_3)_3\text{V}_3\text{W}$ , where X:  $\text{Na}^+$ ,  $\text{K}^+$ ,  $\text{Ca}^{2+}$ ; Y:  $\text{Fe}^{2+}$ ,  $\text{Li}^+$ ,  $\text{Mn}^{2+}$ ,  $\text{Mg}^{2+}$ ,  $\text{Al}^{3+}$ ,  $\text{Cr}^{3+}$ ,  $\text{Fe}^{3+}$ ,  $\text{Ti}^{4+}$ ; Z:  $\text{Al}^{3+}$ ,  $\text{Fe}^{3+}$ ,  $\text{V}^{3+}$ ,  $\text{Fe}^{2+}$ ; T:  $\text{Si}^{4+}$ ,  $\text{Al}^{3+}$ ,  $\text{B}^{3+}$ ; B:  $\text{B}^{3+}$ ; V:  $\text{OH}^-$ ,  $\text{O}^{2-}$ ; W:  $\text{OH}^-$ ,  $\text{O}^{2-}$ ,  $\text{F}^-$  [44-45], which has immense application potential in aspects of environment [39-40], energy [41], and iatrology [43] fields. By virtue of the nature of pyroelectric and piezoelectric [45], the ability of separating photo-generated  $e^-/h^+$  pairs [46-47,40] and the abundant source, tourmaline is an appropriate candidate for photocatalytic application.

It was widely demonstrated that ternary photocatalysts could result in higher photocatalytic property due to synergistic effect of the components [51-52]. For example,  $\text{BiPO}_4$ - $\text{MoS}_2$ -graphene composite showed enhanced photocatalytic activity than that of

BiPO<sub>4</sub>, MoS<sub>2</sub>, and MoS<sub>2</sub>-BiPO<sub>4</sub> composite for photocatalytic degradation of dyes [53]. The photocatalytic activity of the samples was evaluated by degradation of Rhodamine B (RhB) under visible-light irradiation.

## Results and Discussion

The crystal structures of photocatalysts were further characterized by XRD displayed in Fig.1. There was a strong diffraction peak located at  $2\theta = 26.56^\circ$  (Fig. 1a) for graphite, indicating good crystallization nature. The (001) plane of GO showed a broad diffraction peak at  $2\theta = 10.69^\circ$  (Fig. 1b). A broad peak appeared at  $2\theta = 25.22^\circ$  after GO went through hydrothermal reaction (Fig. 1b), suggesting effective deoxygenation of GO [54]. The XRD pattern of tourmaline powders (Fig. 1c) was well indexed to that of Fe-rich tourmaline (JCPDS 85-1811) and no other peak of impurity was observed. The peaks located at  $14.27^\circ$ ,  $33.45^\circ$ ,  $39.55^\circ$ ,  $49.10^\circ$  and  $58.91^\circ$  (Fig. 1d) corresponded to (002), (100), (103), (105) and (110) planes of hexagonal 2H-MoS<sub>2</sub> (JCPDS 37-1492), respectively. In addition, due to the small content of tourmaline in the composite, the diffraction peaks of tourmaline were unresolved for the patterns of MoS<sub>2</sub>-GR-T samples.

Raman spectra were employed to further determine the co-existence of the samples (Fig. 2). Two Raman peaks appeared at  $1350\text{ cm}^{-1}$  and  $1601\text{ cm}^{-1}$  (Fig. 2a) could be assigned to the D band (signal from the disordered carbon) and G band (signal from the sp<sup>2</sup> hybridized carbon). The I<sub>D</sub>/I<sub>G</sub> (I meant the band intensity) ratio of GO, GR and MoS<sub>2</sub>-GR-T samples were 0.96, 1.19 and 1.33, respectively. The increased I<sub>D</sub>/I<sub>G</sub> ratio indicated that small graphene domains have been re-established [55, 62]. For MoS<sub>2</sub>-GR-T sample, the D band of GR shifted to  $1344\text{ cm}^{-1}$  and  $1586\text{ cm}^{-1}$ , respectively, indicating successful

synthesis of ternary MoS<sub>2</sub>-GR-T composite. The peaks appeared at 377 cm<sup>-1</sup> and 403 cm<sup>-1</sup> (Fig. 2b) were originated from the  $E_{2g}^1$  vibration model (Mo and S atoms vibrate along the in-plane direction and oppositely to each other) and  $A_{1g}$  vibration model (S atom vibrate along the perpendicular-to-plane direction) of Mo-S bond, respectively [63-64], and a red shift for the two peaks were observed for MoS<sub>2</sub>-T-GR sample.

The SEM images of morphology of the samples were observed in Fig. 3. As it can be seen in Fig. 3a, there were wrinkles on the surface of GO. The tourmaline was granular appearance particles (Fig. 3b) with the average size of  $\sim$ 600 nm. The pristine MoS<sub>2</sub> was flower-like sphere with a diameter of  $\sim$ 800 nm (Fig. 3c). The introduction of tourmaline resulted in the formation of smaller MoS<sub>2</sub> particles ( $\sim$ 400 nm) (Fig. 3d), synergized with GR to make MoS<sub>2</sub> grow along and dispersed well on the substrates (Fig. 3e). The dispersed MoS<sub>2</sub> sustained the approximately uniform pore structure. Graphene provided sites for nucleation and growth of MoS<sub>2</sub> and prevented MoS<sub>2</sub> from agglomeration to prompt the exposure of active sites.

Fig. 3f shows that the image of TEM and high-resolution TEM (HRTEM) to confirm the basic unit of the flower-like architecture of the pristine MoS<sub>2</sub> was nanosheet ( $\sim$ 20 nm in thickness). The selected area electron diffraction (SAED) image of MoS<sub>2</sub> showed three well-defined dispersed rings (inset of Fig. 3f), indicating good polycrystalline nature. The TEM images of MoS<sub>2</sub>-GR-T sample showed that both tourmaline and MoS<sub>2</sub> were dispersed and intimately attached to the surface of graphene (Fig. 3g), which could contribute to fast transfer and separation of the photo-generated e-/h+ pairs. The lattice fringe arising with length of 0.64 nm and 0.35 nm corresponded to the (002) plane of MoS<sub>2</sub> and (012) plane of tourmaline, respectively.

Surface element composition and chemical status of the as-synthesized samples were investigated by XPS (Fig. 4). As shown in Fig. 4a, the full spectrum of MoS<sub>2</sub>-GR-tourmaline composite suggested that it was consisted of Mo, S, C, and trace amount of O considered as H<sub>2</sub>O adhered on the surface of the composites. The XP C1s of rGO spectrum of the (Figure 5a) is characterized by peaks at binding energies (BEs) of 284.79, 286.84 and 287.47 eV, assigned respectively to the following groups: carbon-carbon/ carbon-hydrogen; carbon singly and doubly bound to oxygen (hydroxyl and carbonyl group); and carbon doubly bonded to oxygen (carboxyl group);[54, 60, 62]. There is no obvious chemical shift and observed compared to GO, proving the reduction reaction of GO was not influence C atom. Relative intensities of the peaks characterizing oxygen-containing groups are significantly less than those of unreduced. Otherwise, in contrast to MoS<sub>2</sub>-GR-T sample, the position of every high-resolution C 1s XPS peak is slightly offset, owing to the introduction of S atom to form C-S binding. The S 2p and Mo 3d spectra of MoS<sub>2</sub> showed four peaks at 161.63 eV (S 2p<sub>3/2</sub>), 162.82 eV (S 2p<sub>1/2</sub>), 228.81 eV (Mo 3d<sub>5/2</sub>) and 231.99 eV (Mo 3d<sub>3/2</sub>) (Fig. 4c and d), suggesting the existence of S<sup>2-</sup> and Mo<sup>4+</sup> [27, 65]. The atomic percentage of Mo and S were 25.30% and 49.42%, respectively, which was almost in consonance with the stoichiometry of MoS<sub>2</sub>. It confirmed that ternary MoS<sub>2</sub>-GR-T composite was successfully fabricated.

The optical properties of the samples were showed in UV-vis diffuse reflectance spectra (Fig. 5a). MoS<sub>2</sub>, MoS<sub>2</sub>-T and MoS<sub>2</sub>-GR-T samples absorbed both UV light and visible light effectively. The adsorption intensity of MoS<sub>2</sub>-T and MoS<sub>2</sub>-GR-T samples in the visible-light region was higher than that of MoS<sub>2</sub>. The calculated band gap energies for MoS<sub>2</sub>, MoS<sub>2</sub>-T and MoS<sub>2</sub>-GR-T samples were 2.01 eV, 1.91 eV and 1.79 eV, respectively (Fig. 5b). The decreased band gap energy meant a high level generation of e<sup>-</sup>/h<sup>+</sup> pairs. Recombination level of the photo-generated e<sup>-</sup>/h<sup>+</sup> pairs was characterized by PL spectra

and photocurrent. PL spectra of the samples excited at 325 nm showed two emission peaks between 360 nm and 500 nm (Fig. 5c), which could be ascribed to recombination of the photo-induced  $e^-/h^+$  pairs. The peak intensity was in the order of  $\text{MoS}_2 > \text{MoS}_2\text{-T} > \text{MoS}_2\text{-GR-T}$ , suggesting the  $e^-/h^+$  pairs separation efficiency decreasing in the order of  $\text{MoS}_2\text{-GR-T} > \text{MoS}_2\text{-T} > \text{MoS}_2$ . Photocurrent density of  $\text{MoS}_2$ ,  $\text{MoS}_2\text{-T}$  and  $\text{MoS}_2\text{-GR-T}$  samples (Fig. 5d) further demonstrated that the ternary composite possessed promoted charge separation efficiency than pristine  $\text{MoS}_2$  and binary  $\text{MoS}_2\text{-T}$ .

$\text{N}_2$  adsorption-desorption isotherms (a) and BJH pore size distribution (b) curves of  $\text{MoS}_2$  and  $\text{MoS}_2\text{-GR-T}$  samples were shown in Fig. 6. The  $\text{N}_2$  adsorption-desorption isotherms of  $\text{MoS}_2$  and  $\text{MoS}_2\text{-GR-T}$  exhibited a type-IV adsorption branch with a H3 hysteresis loop. The Brunauer-Emmett-Teller (BET) specific surface area and total pore volume of  $\text{MoS}_2\text{-GR-T}$  composite were  $46.8 \text{ m}^2 \cdot \text{g}^{-1}$  and  $0.27 \text{ cm}^3 \cdot \text{g}^{-1}$ , respectively, which were much larger than those of  $\text{MoS}_2$  ( $9.0 \text{ m}^2 \cdot \text{g}^{-1}$  and  $0.08 \text{ cm}^3 \cdot \text{g}^{-1}$ ). In addition, the average pore size of  $\text{MoS}_2\text{-GR-T}$  composite was calculated to be 23.41 nm according to the Barrett–Joyner–Halenda (BJH) method, which was smaller than that of pristine  $\text{MoS}_2$  (37.11 nm). The larger BET specific surface area and smaller average pore size of  $\text{MoS}_2\text{-GR-T}$  composite could be ascribed to the dispersion of  $\text{MoS}_2$  on the surface of graphene. The results from  $\text{N}_2$  adsorption-desorption analysis agreed well with that of SEM. The more  $\text{MoS}_2$  dispersed well on the surface of graphene, the richer active sites it exposed.

The photodegradation of RhB was employed as a probe reaction to evaluate the photocatalytic activity of the as-synthesized samples. As shown in Fig. 7a, the adsorption-desorption equilibrium of RhB was established within 60 min in the presence of the as-synthesized samples in the dark. The adsorption capacity of  $\text{MoS}_2\text{-GR-T}$  ( $\geq 48.3\%$ ) composite was larger than that of pristine  $\text{MoS}_2$  (41.9%). The photodegradation rates of RhB with  $\text{MoS}_2$ ,  $\text{MoS}_2\text{-T}(1)$  and  $\text{MoS}_2\text{-GR}(5)\text{-T}(1)$  composites under visible-light

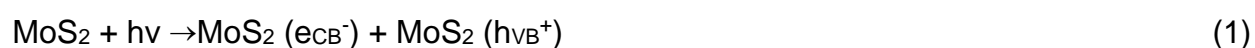
irradiation for 60 min were 68.4%, 72.3% and 93.9%, respectively. The incorporation of graphene and tourmaline improved the photocatalytic activity of MoS<sub>2</sub>. The apparent pseudo-first-order kinetic model was used to analyse the photocatalytic reaction kinetics. The corresponding fitted lines of  $\ln(C_0/C)$  vs. time were exhibited in Fig. 7b. The K (rate constant of pseudo-first-order kinetic equation) values for the degradation reaction of RhB with MoS<sub>2</sub>-T(1)-GR(5), MoS<sub>2</sub>-T(2)-GR(4), MoS<sub>2</sub>-T(3)-GR(3), MoS<sub>2</sub>-T(4)-GR(2), MoS<sub>2</sub>-T(5)-GR(1), MoS<sub>2</sub>, MoS<sub>2</sub>-GR(5) and MoS<sub>2</sub>-T(1) samples were 0.030 min<sup>-1</sup>, 0.027 min<sup>-1</sup>, 0.022 min<sup>-1</sup>, 0.021 min<sup>-1</sup>, 0.016 min<sup>-1</sup>, 0.010 min<sup>-1</sup>, 0.024 min<sup>-1</sup> and 0.012 min<sup>-1</sup>, respectively, best of that was MoS<sub>2</sub>-T(1)-GR(5) composite.

It is of importance to explore the effect of the initial pH of RhB aqueous solution on the photocatalytic degradation rate as the photocatalytic oxidization reaction of dyes usually occurred in aqueous solution. The results showed that the degradation rate decreased with increase of pH (Fig. 7c). RhB is an aromatic amino acid with amphoteric characteristics due to the presence of both amino group and carboxyl group. Therefore, the charge state of RhB depends on pH values of the solution [67-68]. When pH was below 3.10, RhB was positively charged, and when pH was above 3.10, RhB was negatively charged [69]. Results from zeta potential analysis revealed that MoS<sub>2</sub>-GR-T composite was negatively charged with pH varied at the range of 2.02-8.03 (Fig. 7d). Photocatalytic property was affected mainly by the adsorption ability of photocatalysts [70]. When pH was above 2.02 and below 3.10, the adsorption between RhB and MoS<sub>2</sub>-GR-T composite was enhanced mainly by the electrostatic attraction, and when pH was above 3.10, the adsorption between RhB and MoS<sub>2</sub>-T-GR composite was mainly weakened by the electrostatic repulsion.

Major reactive species contributed to the photocatalytic reaction were superoxide radical ( $\bullet\text{O}_2^-$ ), hole ( $h^+$ ) and hydroxyl radical ( $\bullet\text{OH}$ ) [70]. Active species trapping experiments

were carried out to verifying the predominant active species participated in the photodegradation reaction. EDTA, TBA and BQ were employed as  $h^+$ ,  $\bullet OH$  and  $\bullet O^{2-}$  scavengers [71-72], respectively. The degradation rate of RhB decreased with the introduction of EDTA, TBA and BQ (Fig. 8a), which indicated that  $h^+$ ,  $\bullet OH$  and  $\bullet O^{2-}$  contributed to the photocatalytic oxidization reaction. The addition of EDTA, BQ and TBA resulted in the degradation rate decreased from 93.9% to 15.3%, 50.2% and 82.1%, respectively. The results revealed that  $h^+$  and  $\bullet O^{2-}$  were the main reactive species in the photocatalytic system consisted of RhB and MoS<sub>2</sub>-GR-T composite. The EPR spectra of MoS<sub>2</sub>-GR-T composite was carried out to further confirm the formation of  $\bullet O^{2-}$  and  $\bullet OH$ . The characteristic signals of DMPO- $\bullet O^{2-}$  and DMPO- $\bullet OH$  were clearly observed under visible-light irradiation while they were not observed in the dark (Fig. 8b).

Potential mechanism for the enhanced photocatalytic property with the composite was schematically illustrated in Fig. 9. (1) MoS<sub>2</sub> was dispersed well on the surface of graphene and exposed more adsorption-photocatalytic active sites. (2) The optical properties of MoS<sub>2</sub>-T and MoS<sub>2</sub>-GR-T samples were improved compared with pristine MoS<sub>2</sub>. MoS<sub>2</sub>-T and MoS<sub>2</sub>-GR-T samples exhibited strong adsorption property for visible light, which had a positive effect on the photocatalytic property of MoS<sub>2</sub>. (3) The incorporation of graphene and tourmaline synergistically promoted charge separation efficiency. This could be ascribed to the electron-transporting property of graphene and the electron-accepting property of tourmaline [40, 45, 73]. Under light illumination, the  $e^-$  in the valence band (VB) of MoS<sub>2</sub> was excited and transferred to the conduct band (CB). The strong electronic field on the surface of tourmaline made directional transportation of the photo-generated  $e^-$  via graphene to achieve separation of  $e^-/h^+$  pairs. The reactions concerned with the transfer of  $e^-$  in MoS<sub>2</sub>-GR-T composite could be described as follows:





The separated  $e^-$  reacted with the oxygen dissolved in the water to produce superoxide radical anion ( $\bullet\text{O}^{2-}$ ). The generated  $\bullet\text{O}^{2-}$  was a kind of strong oxidants towards the decomposition of organic dyes [74]. Accumulated  $h^+$  on the surface of photocatalyst could oxidize dyes directly [70, 75-76]. Dyes could be degraded in the presence of MoS<sub>2</sub>-T-GR composite.

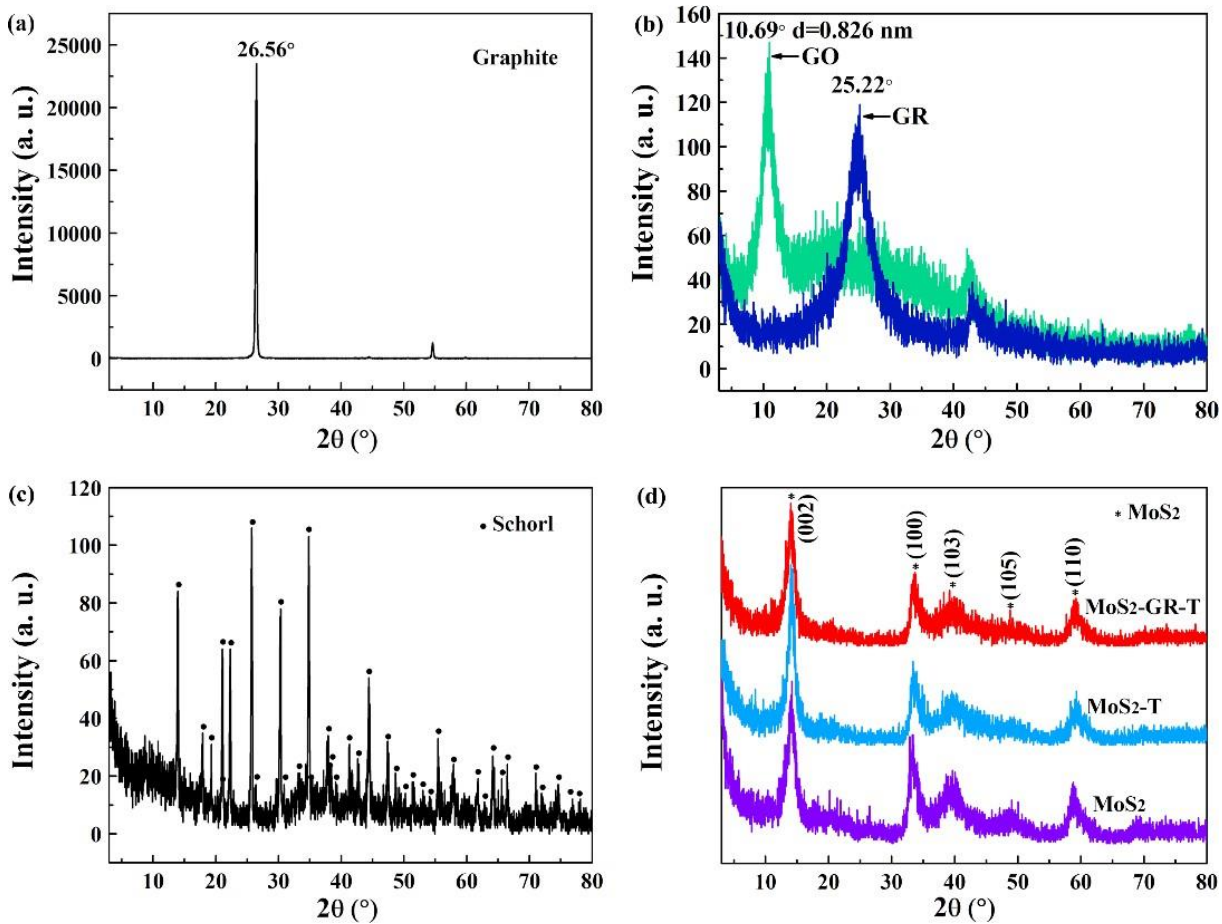


**Fig. 1:** XRD patterns of natural graphite (a), GO and GR (b), tourmaline (c), and MoS<sub>2</sub>, MoS<sub>2</sub>-T and MoS<sub>2</sub>-GR-T samples (d) (color online)

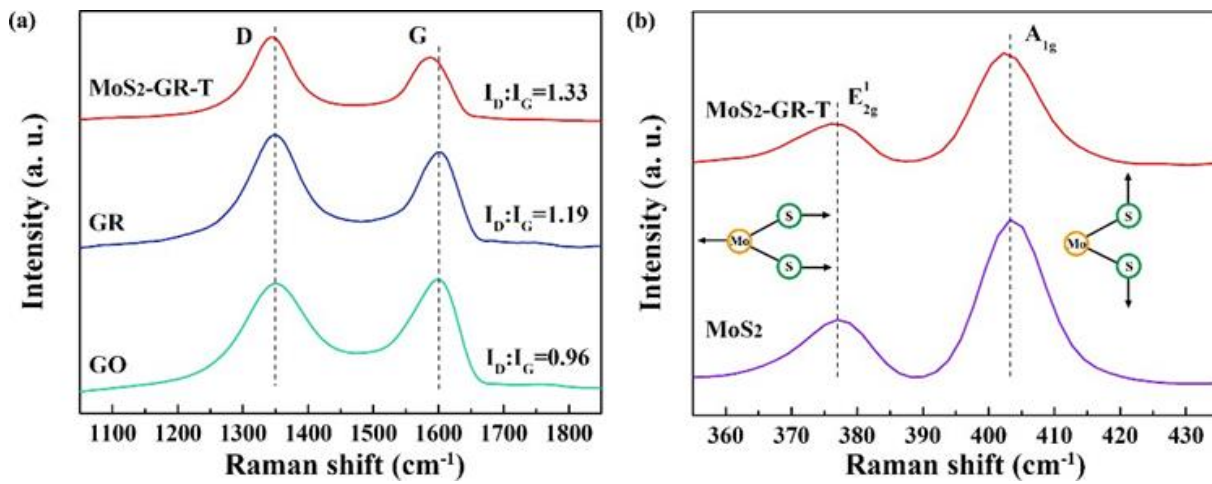


**Fig. 2:** D and G vibration bands for the Raman spectra of GO, GR and MoS<sub>2</sub>-GR-T samples (a); E<sub>2g</sub><sup>1</sup> and A<sub>1g</sub> vibration bands for the Raman spectra of MoS<sub>2</sub> and MoS<sub>2</sub>-GR-T samples (b) (color online).

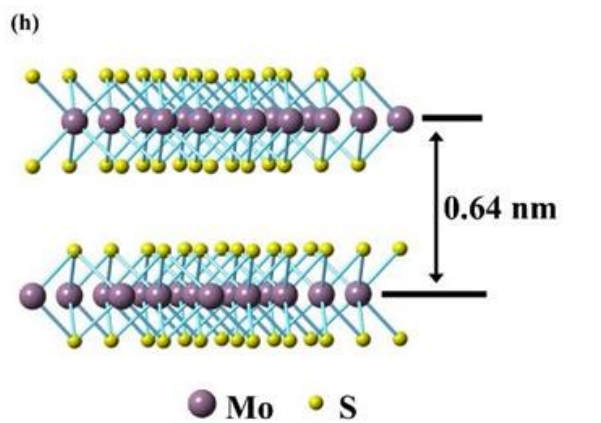
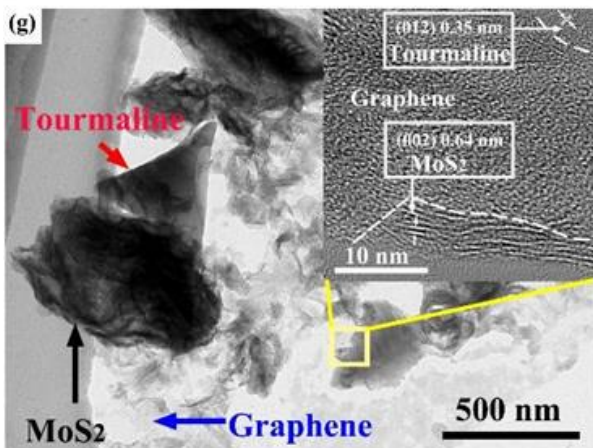
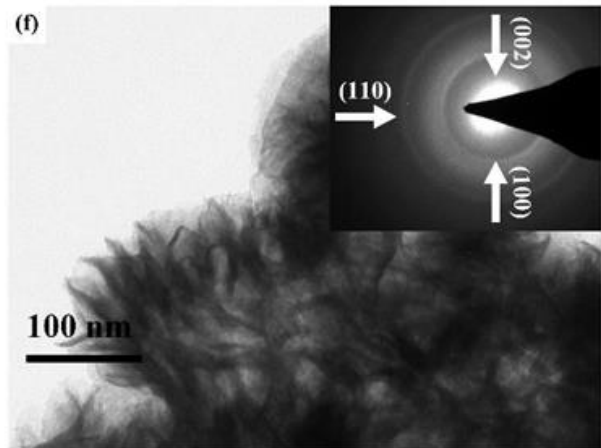
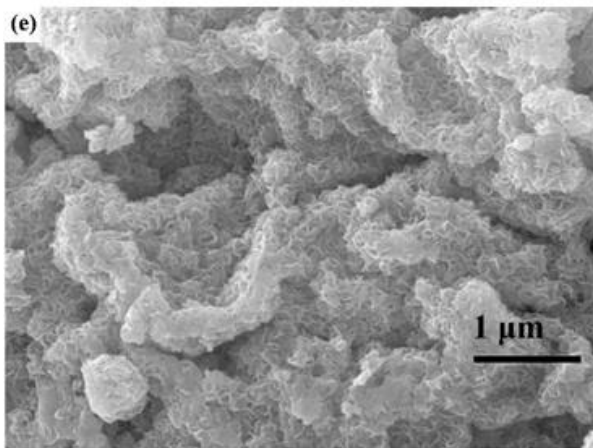
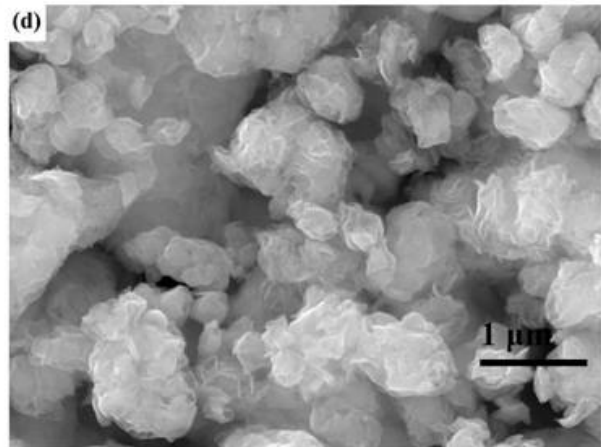
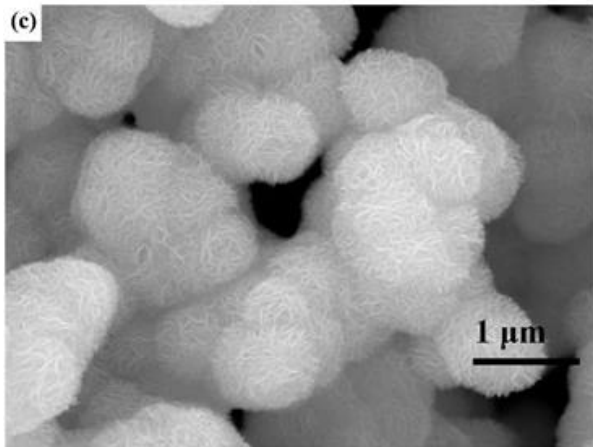
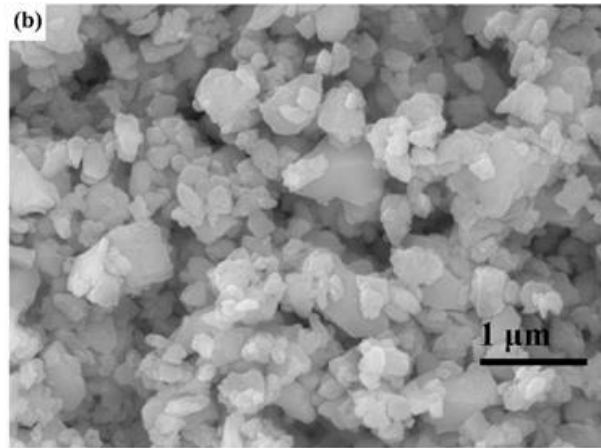
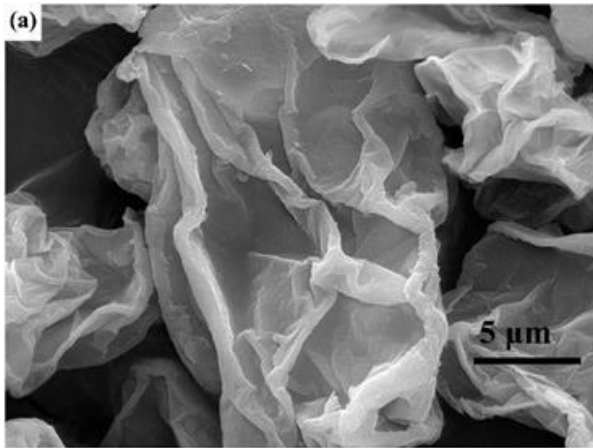


**Fig. 3:** SEM images of GO (a), tourmaline (b), MoS<sub>2</sub> (c), MoS<sub>2</sub>-T (d) and MoS<sub>2</sub>-GR-T samples (e); TEM image of MoS<sub>2</sub>, the inset was the corresponding SAED image (f); TEM image of MoS<sub>2</sub>-GR-T composite, the inset was the corresponding HRTEM image (g); Structural model of MoS<sub>2</sub> (h) (color online)

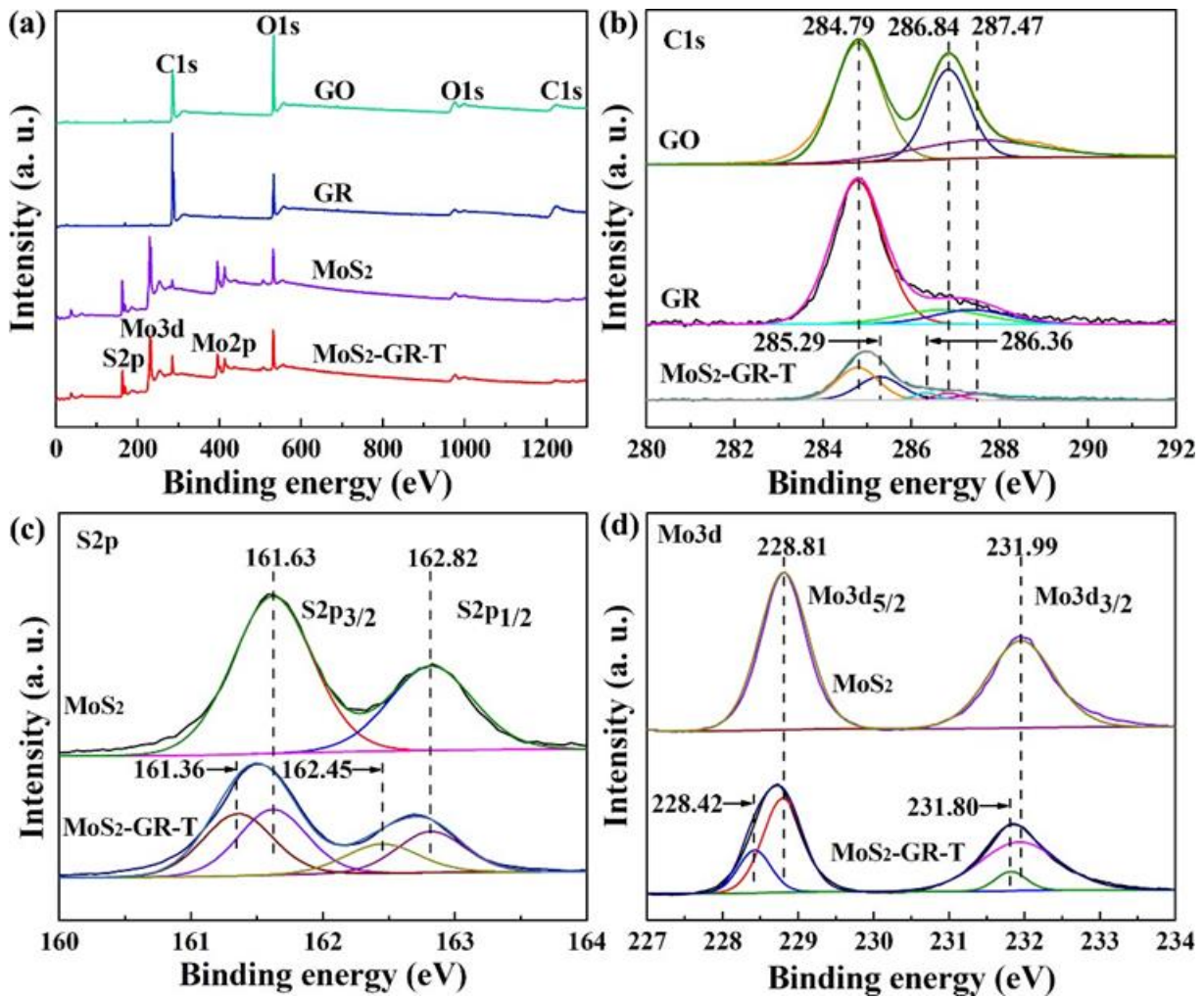


**Fig. 4:** XPS survey spectra (a) and XPS full spectra of C 1s (b), S 2p (c) and Mo 3d (d) of the obtained samples (color online).

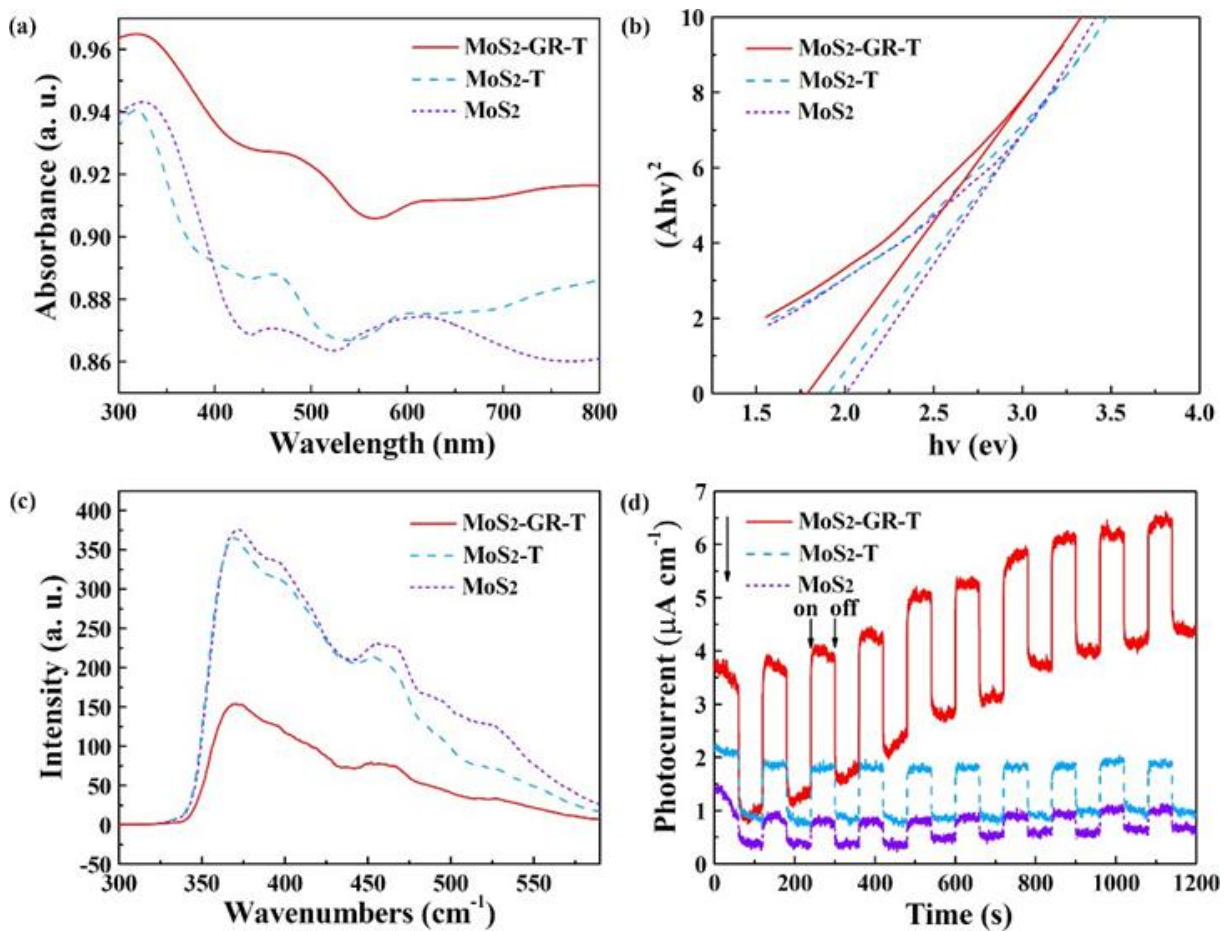


**Fig. 5:** UV-vis diffuse reflectance (a) and the corresponding plots of  $(Ah\nu)^2$  vs. photon energy ( $h\nu$ ) (b); PL spectra (c) and photocurrent curves (d) of MoS<sub>2</sub>, MoS<sub>2</sub>-T and MoS<sub>2</sub>-GR-T samples (color online).

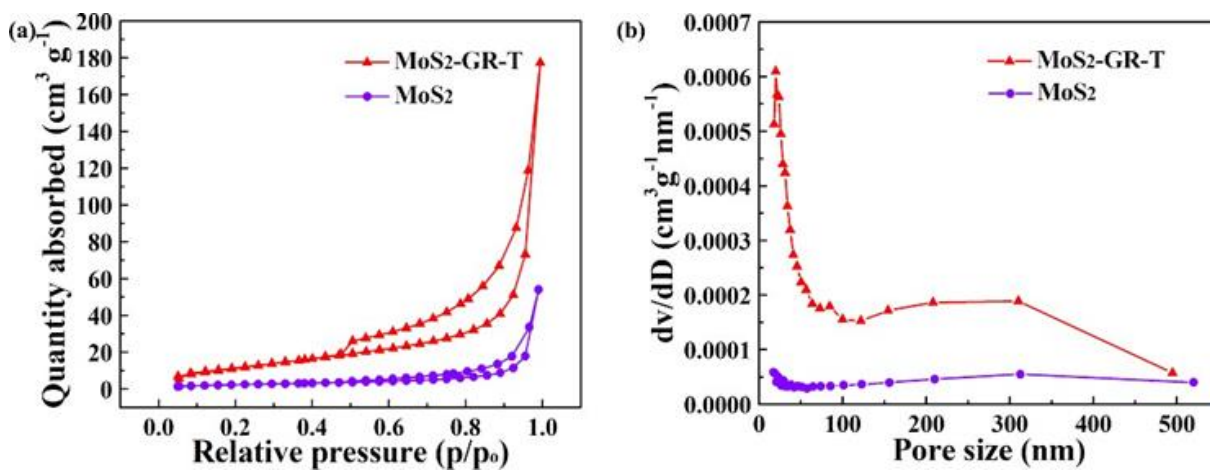


**Fig. 6:**  $N_2$  adsorption-desorption isotherms (a) and BJH pore size distribution (b) curves of MoS<sub>2</sub> and MoS<sub>2</sub>-GR-T samples (color online).

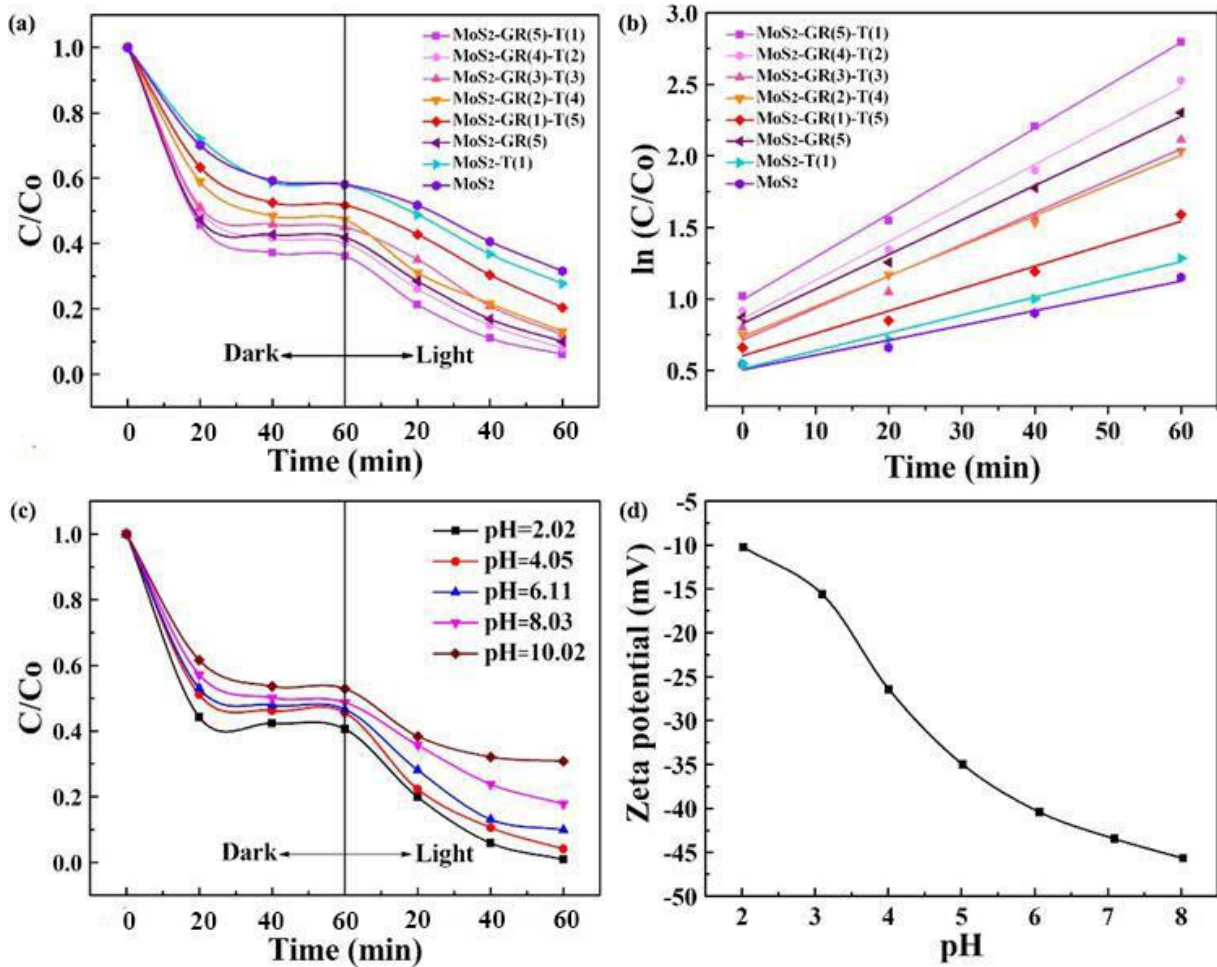


**Fig. 7:** Photocatalytic degradation curves of RhB using MoS<sub>2</sub>, MoS<sub>2</sub>-T, MoS<sub>2</sub>-GR and MoS<sub>2</sub>-GR-T samples with different mass ratio of tourmaline and graphene (a); Apparent pseudo-first-order kinetic plots of ln (C<sub>0</sub>/C) vs. time for photodegradation of RhB with the as-prepared catalysts (b); Effect of the initial pH values of RhB aqueous solution on the photocatalytic property (c) and on the Zeta potential(d) of MoS<sub>2</sub>-GR(5)-T(1) composite (color online)

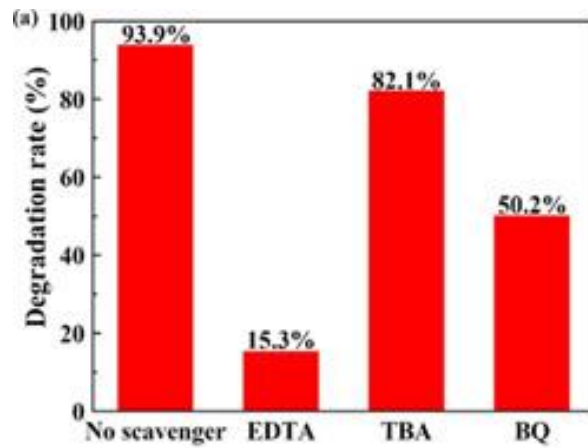


**Fig. 8:** Effect of EDTA, TBA and BQ scavengers on the photocatalytic degradation rate of RhB

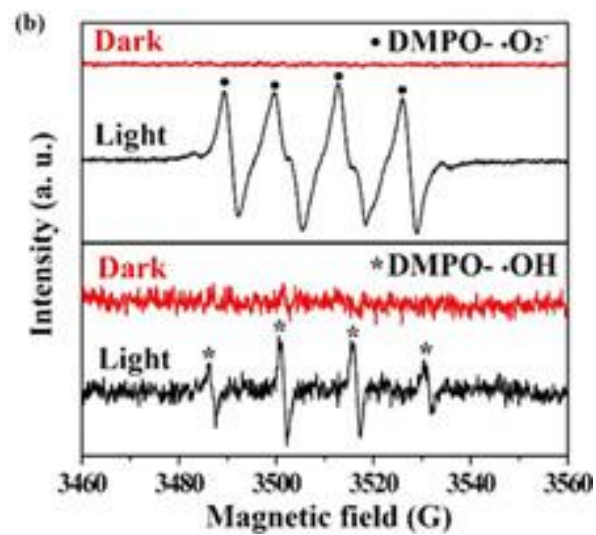


**Fig. 9:** EPR signals of DMPO- $\cdot\text{O}_2^-$  and DMPO- $\cdot\text{OH}$  (b) with MoS<sub>2</sub>-GR-T photocatalyst under visible-light irradiation (color online)

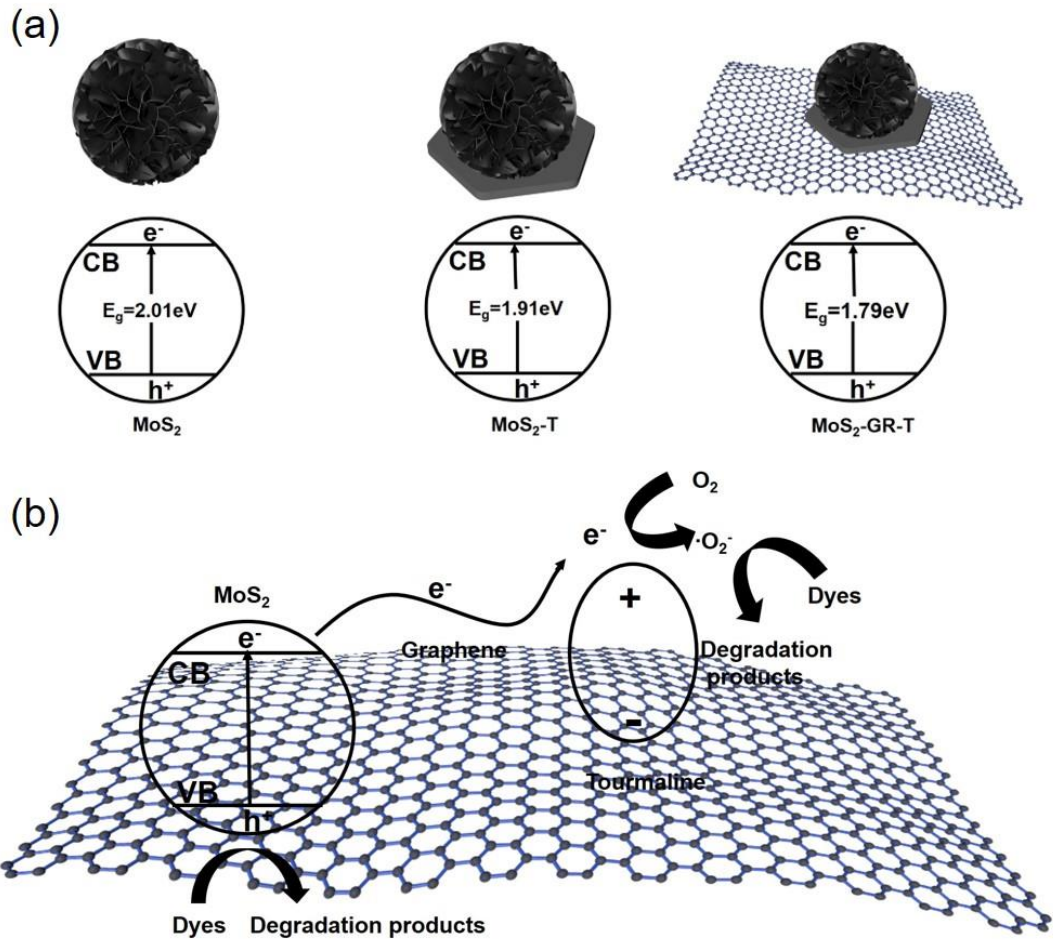


**Fig. 10:** The image of energy band of MoS<sub>2</sub>, MoS<sub>2</sub>-T and MoS<sub>2</sub>-GR-T (a) and the possible reaction mechanism of the ternary MoS<sub>2</sub>-GR-T composite for RhB degradation under visible light irradiation (b)

## Conclusion

In this study, MoS<sub>2</sub>-GR-T composite photocatalyst was successfully synthesized by hydrothermal method. MoS<sub>2</sub> was dispersed well on graphene and exposed more adsorption-photocatalytic active sites. The bandgap energies of MoS<sub>2</sub>, MoS<sub>2</sub>-T and MoS<sub>2</sub>-GR-T samples were 2.01 eV, 1.91 eV and 1.79 eV, respectively. Photocatalytic degradation rates of RhB with MoS<sub>2</sub>, MoS<sub>2</sub>-T and MoS<sub>2</sub>-GR-T samples under visible-light irradiation for 60 min were 68.4%, 72.3% and 93.9%, respectively. Active species trapping experiments and electron paramagnetic resonance spectra revealed that h<sup>+</sup> and •O<sup>-</sup> were the main active species generated by MoS<sub>2</sub>-GR-T composite. The enhanced photocatalytic activity of MoS<sub>2</sub>-GR-T composite could be attributed to the exposed adsorption-photocatalytic active sites, the improved light adsorption ability and the promoted charge separation efficiency. This study provided a new insight to enhance the photocatalytic property of MoS<sub>2</sub> under the synergetic effect of graphene and tourmaline.

## Experimental

Experimental text

### 2.1. Materials

Natural flake graphite powder with purity of about 99.99 wt% was obtained from Shimen, Hunan province, China. The tourmaline sample was obtained from Hebei province, China. Tourmaline particles were rinsed with distilled water, dried at 70 °C and was grinded with a planetary mill. The ground tourmaline powders were sieved

(325 mesh) to obtain grain sizes  $\leq 45 \mu\text{m}$ . The sieved tourmaline powders were immersed in water followed by magnetic stirring for 2 h, filtered and dried at  $70 \text{ }^\circ\text{C}$ .

Potassium permanganate ( $\text{KMnO}_4$ , 99.5%), concentrated sulfuric acid ( $\text{H}_2\text{SO}_4$ , 95.0%~98.0%), hydrogen peroxide ( $\text{H}_2\text{O}_2$ , 30%) and thiourea ( $\text{CH}_4\text{N}_2\text{S}$ , 99.0%) were purchased from Sinopharm Group Chemical Reagent Co. Ltd., China. Sodium nitrate ( $\text{NaNO}_3$ , 99.0%) was purchased from Shantou Xilong Chemical Co Ltd., China. Hydrochloric acid ( $\text{HCl}$ , 36.0%~38.0%) was purchased from Hunan Zhuzhou Xingkong Glass Co, Ltd., China. Sodium molybdate ( $\text{Na}_2\text{MoO}_4 \cdot 2\text{H}_2\text{O}$ , 99.0%) was obtained from Guangdong Guanghua SciTech Co. Ltd, China. 5, 5-dimethyl-1-pyrroline N-oxide (DMPO, 97%), disodium ethylenediaminetetraacetate (EDTA, 99%), tert-butyl alcohol (TBA, 99.5%), 1,4-benzoquinone (BQ, 98%), nafion (5%), sodium sulphite anhydrous ( $\text{Na}_2\text{SO}_3$ , 98%) and sodium sulfide ( $\text{Na}_2\text{S}$ , 95%) were supplied by Aladdin Chemistry Co. Ltd, China. All the reagents were analytical grade and were used as received without further purification. Doubly distilled water was used throughout this study.

## **2.2. Synthesis of graphene oxide**

The graphene oxide (GO) used in this work was prepared via an ultrasound-assisted modified Hummer's method. In detail: 1 g of natural flake graphite powder, 1 g of  $\text{NaNO}_3$ , 6 g of  $\text{KMnO}_4$  and 46 ml of concentrated  $\text{H}_2\text{SO}_4$  were added into a beaker and the obtained mixture was immersed in ice water, magnetically stirred for 2 h. The temperature of the mixture was maintained at  $35 \text{ }^\circ\text{C}$  by water bath for 30 min. 92 ml of distilled water was then added into above mixture and the temperature was kept at  $98 \text{ }^\circ\text{C}$  for 15 min. The obtained brown paste was diluted with 280 ml of distilled water and was treated with 20 ml of  $\text{H}_2\text{O}_2$  until color of the suspension turn into bright yellow. The suspension was then rinsed with 5%  $\text{HCl}$  aqueous solution and a large amount of

distilled water until the  $\text{pH}=7\pm 0.3$ . Finally, the obtained bright yellow slurry was dispersed in distilled water and sonicated for 4 h to obtain GO aqueous colloid. The GO aqueous colloid was dried using a freezing dryer and the resultant product was ground into powders in the agate mortar.

### **2.3. Synthesis of the samples**

$\text{MoS}_2$ -GR-T composites were synthesized via a hydrothermal method. In detail: 0.0120 g of GO powders and 0.0024 g of tourmaline powders were mixed with 60 ml of distilled water to form a homogeneous suspension after stirring 30 min and ultrasonic-assisted for 1 h. The obtained suspension sealed at a 100 ml of Teflon-lined autoclave and maintained at 220 °C for 24 h by adding 0.3630 g of  $\text{Na}_2\text{MoO}_4 \cdot 2\text{H}_2\text{O}$  and 0.3510 g of  $\text{CH}_4\text{N}_2\text{S}$ . Finally, the resultant product was rinsed with distilled water and dried at 70 °C, labelled as  $\text{MoS}_2$ -GR(5)-T(1). At the same weight of  $\text{MoS}_2$ , different  $\text{MoS}_2$ -GR-T composites were achieved by adjusting the mass ratio of tourmaline and GO.  $\text{MoS}_2$ ,  $\text{MoS}_2$ -GR(5) and  $\text{MoS}_2$ -T(1) samples were synthesized in the same method without the addition of tourmaline and GO, tourmaline and GO, respectively.

### **2.4. Characterization**

The X-ray diffraction (XRD) patterns were obtained using a DX-2700 diffractometer (Dandong Haoyuan Instrument Co. Ltd., China) with Ni-filtered  $\text{CuK}\alpha 1$  ( $\lambda=1.5405 \text{ \AA}$ ), 40 kV accelerating voltage and 40 mA current. Raman spectra were performed under 532 nm laser using an inVia spectrometer (Renishaw, UK). Scanning electron microscopy (SEM) images were obtained on a MIRA3 instrument (Tescan, Czech). Microstructure of the samples was studied using a Titan G2 60-300 transmission electron microscope (TEM, FEI, USA). X-ray photoelectron spectra (XPS) were

performed on an ESCALAB 250Xi instrument (ThermoFisher Scientific, USA). UV-visible diffuse reflectance spectra were measured using a Lambda 750S UV-vis spectrophotometer (Perkin-Elmer, USA). Photoluminescence (PL) spectra were obtained using a F-4500 fluorescence spectrophotometer (Hitachi, Japan). Two Interface 1010E electrochemical workstation (Gamry, USA) was employed to measure photocurrent using  $\text{Na}_2\text{SO}_3$  (0.1 M) and  $\text{Na}_2\text{S}$  (0.1 M) solutions with volume ratio of 1:1 as electrolyte under LED lamp ( $\lambda=470$  nm) irradiation.  $\text{N}_2$  adsorption-desorption isotherms were obtained using an ASAP 2020 surface area analyzer (Micromeritics, USA). Zeta potential measurement was carried out on a Zetasizer Nano Zs90 instrument (Malvern, UK). Electron paramagnetic resonance (EPR) was analyzed using an A300 spectrometer (Bruker, Germany) with DMPO as free radical scavenger.

## **2.5. Photocatalytic and trapping experiments**

Photocatalytic property of the as-synthesized samples was evaluated as follows: 50 mg of the as-synthesized samples were mixed with 100 ml of  $5 \text{ mg}\cdot\text{L}^{-1}$  RhB aqueous solution and the obtained suspension was stirred in the dark. 4 ml of the suspension were extracted every 20 min and was centrifuged to acquire the clarified solution. Absorbance of the solution was measured using a unico 2600 UV-vis spectrophotometer at 554 nm wavelength. Adsorption experiments were proceeded until the adsorption-desorption equilibrium had been established. Then the suspension was exposed to visible-light resource (A 300 W Xe lamp with an UV cut-off filter).

Trapping experiments were carried out the same as photocatalytic experiments except for addition of 2 ml of EDTA (1 mM), TBA (1 mM) and BQ (1 mM) solutions before light irradiation. Progress of the photocatalytic reaction was monitored by measuring absorbance of the clarified solution. Degradation rate (%) was calculated based on the

formula: degradation rate (%) =  $(A_0 - A) / A_0 \times 100\%$ , where  $A_0$  is the initial absorbance of RhB aqueous solution and  $A$  is absorbance of the resultant solution at predetermined time intervals.

## Supporting Information

Supporting Information File 1

File Name: Additional characterization data

## Acknowledgements

This work was financially supported by the National Twelfth Five-year Science and Technology Support Program of China (2012BAB10B00). We also thank the support of the Fundamental Research Funds for the Central Universities of Central South University (2019zzts692) and National Training Program of Innovation and Entrepreneurship for Undergraduates (502321033).

## References

- 1 Wu, T.; Wang, P.; Ao, Y. *Journal of Wuhan University of Technology-Materials Science Edition*, **2019**, *34*, 521-526. 10.1007/s11595-019-2082-2
- 2 Du, J.; Wang, Z.; Li, Y.; Li, R.; Li, X.; Wang, K. **2019**, 1167-1173.
- 3 Yang, X.; Chen, B.; Chen, J.; Zhang, Y.; Liu, W.; Sun, Y. *Materials Science in Semiconductor Processing*, **2018**, *74*, 309-312. 10.1016/j.mssp.2017.08.011
- 4 Hernandez Castillo, R.; Acosta, M.; Riech, I.; Santana-Rodriguez, G.; Mendez-Gamboa, J.; Acosta, C.; Zambrano, M. *Optik*, **2017**, *148*, 95-100. 10.1016/j.ijleo.2017.09.002
- 5 Zhao, H.; Wu, J.; Li, J.; Wu, H.; Zhang, Y.; Liu, H. *Applied Surface Science*, **2018**, *462*, 337-343. 10.1016/j.apsusc.2018.08.110
- 6 Son, Y.; Lee, J.-S.; Choi, M.; Son, Y.; Park, N.; Ko, M.; Jang, J.-H.; Park,

- M. *Applied Surface Science*, **2018**, *459*, 98-104. 10.1016/j.apsusc.2018.07.027
- 7 Lin, S.; Yang, Z.; Yue, H.; He, D. *Materials Letters*, **2015**, *158*, 9-12.  
10.1016/j.matlet.2015.05.051
- 8 Ren, Y.; Lv, W.; Wen, F.; Xiang, J.; Liu, Z. *Materials Letters*, **2016**, *174*, 24-  
27. 10.1016/j.matlet.2016.03.075
- 9 Ma, L.; Zhang, Q.; Wu, C.; Zhang, Y.; Zeng, L. *Analytica Chimica Acta*, **2019**,  
*1055*, 17-25. 10.1016/j.aca.2018.12.025
- 10 Rana, M.; Chowdhury, P. *Journal of Luminescence*, **2019**, *206*, 105-112.  
10.1016/j.jlumin.2018.10.060
- 11 Chang, C. J.; Wei, Y.-H.; Huang, K.-P. *International Journal of Hydrogen  
Energy*, **2017**, *42*, 23578-23586. 10.1016/j.ijhydene.2017.04.219
- 12 Park, J.-H.; Ramasamy, P.; Kim, S.; Kim, Y. K.; Ahilan, V.; Shanmugama,  
S.; Lee, J.-S. *Chemical Communications*, **2017**, *53*, 3277-3280.  
10.1039/c7cc00071e
- 13 Dai, W.; Yu, J.; Deng, Y.; Hu, X.; Wang, T.; Luo, X. *Applied Surface  
Science*, **2017**, *403*, 230-239. 10.1016/j.apsusc.2017.01.171
- 14 Xu, F.; Zhu, B.; Cheng, B.; Yu, J.; Xu, J. *Advanced Optical Materials*, **2018**,  
*6*. 10.1002/adom.201800911
- 15 Sharma, V.; Maivizhikannan, V.; Rao, V. N.; Kumar, S.; Kumar, A.; Kumar,  
A.; Shankar, M. V.; Krishnan, V. *Ceramics International*, **2020**.  
<https://doi.org/10.1016/j.ceramint.2020.09.199>
- 16 Eda, G.; Yamaguchi, H.; Voiry, D.; Fujita, T.; Chen, M.; Chhowalla, M. *Nano Letters*, **2011**, *11*, 5111-5116. 10.1021/nl201874w
- 17 Parzinger, E.; Miller, B.; Blaschke, B.; Garrido, J. A.; Ager, J. W.; Holleitner,  
A.; Wurstbauer, U. *Acs Nano*, **2015**, *9*, 11302-11309.  
10.1021/acsnano.5b04979
- 18 King, L. A.; Zhao, W.; Chhowalla, M.; Riley, D. J.; Eda, G. *Journal of  
Materials Chemistry A*, **2013**, *1*, 8935-8941. 10.1039/c3ta11633f
- 19 Peng, K.; Fu, L.; Yang, H.; Ouyang, J.; Tang, A. *Nano Research*, **2016**, *10*,  
570-583. 10.1007/s12274-016-1315-3
- 20 Radisavljevic, B.; Radenovic, A.; Brivio, J.; Giacometti, V.; Kis, A. *Nat  
Nanotechnol*, **2011**, *6*, 147-150. 10.1038/nnano.2010.279
- 21 Mak, K. F.; Lee, C.; Hone, J.; Shan, J.; Heinz, T. F. *Phys Rev Lett*, **2010**,  
*105*, 136805. 10.1103/PhysRevLett.105.136805
- 22 Mak, K. F.; He, K.; Lee, C.; Lee, G. H.; Hone, J.; Heinz, T. F.; Shan, J. *Nature Materials*, **2013**, *12*, 207-211. 10.1038/nmat3505
- 23 Chhowalla, M.; Shin, H. S.; Eda, G.; Li, L.-J.; Loh, K. P.; Zhang, H. *Nature  
Chemistry*, **2013**, *5*, 263-275. 10.1038/nchem.1589
- 24 Yang, L.; Guo, S.; Li, X. *Journal of Alloys and Compounds*, **2017**, *706*, 82-88.  
10.1016/j.jallcom.2017.02.240
- 25 Xu, H.; Yi, J.; She, X.; Liu, Q.; Song, L.; Chen, S.; Yang, Y.; Song, Y.;  
Vajtai, R.; Lou, J.; Li, H.; Yuan, S.; Wu, J.; Ajayan, P. M. *Applied Catalysis  
B: Environmental*, **2018**, *220*, 379-385. 10.1016/j.apcatb.2017.08.035
- 26 Yuan, Y.-J.; Yu, Z.-T.; Li, Y.-H.; Lu, H.-W.; Chen, X.; Tu, W.-G.; Ji, Z.-G.;  
Zou, Z.-G. *Applied Catalysis B-Environmental*, **2016**, *181*, 16-23.

- 10.1016/j.apcatb.2015.07.030
- 27 Wang, Y.; Sun, M.; Fang, Y.; Sun, S.; He, J. *Journal of Materials Science*, **2016**, *51*, 779-787. 10.1007/s10853-015-9401-6
- 28 Peng, K.; Fu, L.; Ouyang, J.; Yang, H. *Advanced Functional Materials*, **2016**, *26*, 2666-2675. 10.1002/adfm.201504942
- 29 Zhou, W.; Zhou, K.; Hou, D.; Liu, X.; Li, G.; Sang, Y.; Liu, H.; Li, L.; Chen, S. *ACS Appl Mater Interfaces*, **2014**, *6*, 21534-21540. 10.1021/am506545g
- 30 Cao, Y.; Gao, Q.; Li, Q.; Jing, X.; Wang, S.; Wang, W. *RSC Advances*, **2017**, *7*, 40727-40733. 10.1039/c7ra06774g
- 31 Xiang, Q.; Yu, J. *J Phys Chem Lett*, **2013**, *4*, 753-759. 10.1021/jz302048d
- 32 Xiang, Q.; Yu, J.; Jaroniec, M. *Chemical Society Reviews*, **2012**, *41*, 782-796. 10.1039/c1cs15172j
- 33 Xu, D.; Cheng, B.; Wang, W.; Jiang, C.; Yu, J. *Applied Catalysis B-Environmental*, **2018**, *231*, 368-380. 10.1016/j.apcatb.2018.03.036
- 34 Ding, Y.; Zhou, Y.; Nie, W.; Chen, P. *Applied Surface Science*, **2015**, *357*, 1606-1612. 10.1016/j.apsusc.2015.10.030
- 35 Zhao, Y.; Zhang, X.; Wang, C.; Zhao, Y.; Zhou, H.; Li, J.; Jin, H. *Applied Surface Science*, **2017**, *412*, 207-213. 10.1016/j.apsusc.2017.03.181
- 36 Yuan, Y.; Shen, P.; Li, Q.; Chen, G.; Zhang, H.; Zhu, L.; Zou, B.; Liu, B. *Journal of Alloys and Compounds*, **2017**, *700*, 12-17. 10.1016/j.jallcom.2017.01.027
- 37 Chang, K.; Mei, Z.; Wang, T.; Kang, Q.; Ouyang, S.; Ye, J. *Acs Nano*, **2014**, *8*, 7078-7087. 10.1021/nn5019945
- 38 Li, J.; Wang, C.; Wang, D.; Zhou, Z.; Sun, H.; Zhai, S. *Chemical Engineering Journal*, **2016**, *296*, 319-328. 10.1016/j.cej.2016.03.118
- 39 Li, K.; Chen, T.; Yan, L.; Dai, Y.; Huang, Z.; Guo, H.; Jiang, L.; Gao, X.; Xiong, J.; Song, D. *Catalysis Communications*, **2012**, *28*, 196-201. 10.1016/j.catcom.2012.09.008
- 40 Zhu, D.; Liang, J.; Ding, Y.; Xu, A. *Journal of Nanoscience and Nanotechnology*, **2010**, *10*, 1676-1680. 10.1166/jnn.2010.2070
- 41 Xue, G.; Han, C.; Liang, J.; Wang, S.; Zhao, C. *Journal of Nanoscience and Nanotechnology*, **2014**, *14*, 3943-3947. 10.1166/jnn.2014.7983
- 42 Tijjing, L. D.; Ruelo, M. T. G.; Amarjargal, A.; Pant, H. R.; Park, C.-H.; Kim, D. W.; Kim, C. S. *Chemical Engineering Journal*, **2012**, *197*, 41-48. 10.1016/j.cej.2012.05.005
- 43 Yeredla, R. R.; Xu, H. *Journal of Physical Chemistry C*, **2008**, *112*, 532-539. 10.1021/jp076824l
- 44 Bian, X.; Ji, R. *Desalination and Water Treatment*, **2016**, *57*, 19292-19300. 10.1080/19443994.2015.1096831
- 45 Bian, X.; Chen, J.; Ji, R. *Materials*, **2013**, *6*, 1530-1542. 10.3390/ma6041530
- 46 Zhu, D.; Liang, J.; Ding, Y.; Xue, G.; Liu, L. *Journal of the American Ceramic Society*, **2008**, *91*, 2588-2592. 10.1111/j.1551-2916.2008.02487.x
- 47 Zhu, D.; Xu, A.; Liang, J. *Journal of Nanoscience and Nanotechnology*, **2011**, *11*, 9594-9599. 10.1166/jnn.2011.5274

- 48 Liang, J.-S.; Meng, J.-P.; Liang, G.-C.; Feng, Y.-W.; Ding, Y. *Transactions of Nonferrous Metals Society of China*, **2006**, *16*, S542-S546. 10.1016/s1003-6326(06)60253-7
- 49 Chen, L.; He, F.; Zhao, N.; Guo, R. *Applied Surface Science*, **2017**, *420*, 669-680. 10.1016/j.apsusc.2017.05.099
- 50 Qin, N.; Xiong, J.; Liang, R.; Liu, Y.; Zhang, S.; Li, Y.; Li, Z.; Wu, L. *Applied Catalysis B: Environmental*, **2017**, *202*, 374-380. <https://doi.org/10.1016/j.apcatb.2016.09.040>
- 51 Lv, H.; Liu, Y.; Tang, H.; Zhang, P.; Wang, J. *Applied Surface Science*, **2017**, *425*, 100-106. 10.1016/j.apsusc.2017.06.303
- 52 Zhang, Q.; Tian, C.; Wu, A.; Tan, T.; Sun, L.; Wang, L.; Fu, H. *Journal of Materials Chemistry*, **2012**, *22*, 11778-11784. 10.1039/c2jm31401k
- 53 Yang, J.; Tian, C.; Wang, L.; Fu, H. *Journal of Materials Chemistry*, **2011**, *21*, 3384-3390. 10.1039/c0jm03361h
- 54 Nethravathi, C.; Rajamathi, M. *Carbon*, **2008**, *46*, 1994-1998. 10.1016/j.carbon.2008.08.013
- 55 Wang, Y.; Li, Z.; He, Y.; Li, F.; Liu, X.; Yang, J. *Materials Letters*, **2014**, *134*, 115-118. 10.1016/j.matlet.2014.07.076
- 56 Pulido, A.; Concepcion, P.; Boronat, M.; Botas, C.; Alvarez, P.; Menendez, R.; Corma, A. *Journal of Materials Chemistry*, **2012**, *22*, 51-56. 10.1039/c1jm14514b
- 57 Wang, S.; Liu, B.; Zhi, G.; Gong, X.; Zhang, J. *Applied Surface Science*, **2018**, *458*, 954-963. <https://doi.org/10.1016/j.apsusc.2018.07.075>
- 58 Fan, J.; Liu, S.; Yu, J. *Journal of Materials Chemistry*, **2012**, *22*, 17027-17036. 10.1039/c2jm33104g
- 59 Castaneda, C.; Oliveira, E. F.; Gomes, N.; Soares, A. C. P. *American Mineralogist*, **2000**, *85*, 1503-1507. 10.2138/am-2000-1021
- 60 Huang, Q.; Fang, Y.; Shi, J.; Liang, Y.; Zhu, Y.; Xu, G. *Acs Applied Materials & Interfaces*, **2017**, *9*, 36431-36437. 10.1021/acsami.7b11940
- 61 Hu, X.; Deng, F.; Huang, W.; Zeng, G.; Luo, X.; Dionysiou, D. D. *Chemical Engineering Journal*, **2018**, *350*, 248-256. 10.1016/j.cej.2018.05.182
- 62 Zhang, H.; Fan, X.; Quan, X.; Chen, S.; Yu, H. *Environmental Science & Technology*, **2011**, *45*, 5731-5736. 10.1021/es2002919
- 63 Vattikuti, S. V. P.; Byon, C. *Superlattices and Microstructures*, **2016**, *100*, 514-525. 10.1016/j.spmi.2016.10.012
- 64 Huang, Y.; Zheng, X.; Feng, S.; Guo, Z.; Liang, S. *Colloids and Surfaces a-Physicochemical and Engineering Aspects*, **2016**, *489*, 154-162. 10.1016/j.colsurfa.2015.10.050
- 65 Li, L.; Liu, S.; Zhu, T. *Journal of Environmental Sciences*, **2010**, *22*, 1273-1280. 10.1016/s1001-0742(09)60250-3
- 66 Isari, A. A.; Payan, A.; Fattahi, M.; Jorfi, S.; Kakavandi, B. *Applied Surface Science*, **2018**, *462*, 549-564. 10.1016/j.apsusc.2018.08.133
- 67 Tan, Y.; Yu, K.; Yang, T.; Zhang, Q.; Cong, W.; Yin, H.; Zhang, Z.; Chen, Y.; Zhu, Z. *Journal of Materials Chemistry C*, **2014**, *2*, 5422-5430. 10.1039/c4tc00423j

- 68 Li, J.; Liu, E.; Ma, Y.; Hu, X.; Wan, J.; Sun, L.; Fan, J. *Applied Surface Science*, **2016**, *364*, 694-702. 10.1016/j.apsusc.2015.12.236
- 69 Tian, N.; Huang, H.; He, Y.; Guo, Y.; Zhang, T.; Zhang, Y. *Dalton Transactions*, **2015**, *44*, 4297-4307. 10.1039/c4dt03905j
- 70 Shi, L.; He, Z.; Liu, S. *Applied Surface Science*, **2018**, *457*, 30-40. 10.1016/j.apsusc.2018.06.132
- 71 Neelgund, G. M.; Oki, A. *Acs Omega*, **2017**, *2*, 9095-9102. 10.1021/acsomega.7b01398
- 72 Wu, X.; Hu, Y.; Wang, Y.; Zhou, Y.; Han, Z.; Jin, X.; Chen, G. *Applied Surface Science*, **2019**, *464*, 108-114. 10.1016/j.apsusc.2018.09.059
- 73 Su, F.; Mathew, S. C.; Lipner, G.; Fu, X.; Antonietti, M.; Blechert, S.; Wang, X. *Journal of the American Chemical Society*, **2010**, *132*, 16299-16301. 10.1021/ja102866p
- 74 Li, Q.; Zhang, N.; Yang, Y.; Wang, G.; Ng, D. H. L. *Langmuir*, **2014**, *30*, 8965-8972. 10.1021/la502033t
- 75 Yu, C.; Wen, M.; Tong, Z.; Li, S.; Yin, Y.; Liu, X.; Li, Y.; Liang, T.; Wu, Z.; Dionysiou, D. D. *Beilstein Journal of Nanotechnology*, **2020**, *11*, 407-416. 10.3762/bjnano.11.31
- 76 Sun, X.-Y.; Zhang, X.; Sun, X.; Qian, N.-X.; Wang, M.; Ma, Y.-Q. *Beilstein Journal of Nanotechnology*, **2019**, *10*, 2116-2127. 10.3762/bjnano.10.206